Sensors & Diagnostics

PAPER

View Article Online
View Journal | View Issue

Cite this: *Sens. Diagn.*, 2025, **4**, 63

Biocompatible luminescent Ce^{3+}-sensitized SrF_2: Tb^{3+} for anticounterfeiting and forensic fingerprint detection

Dhanapriya Devi Yengkhom,[a] Henasurkishore Oinam,[a] Silvia Thongbram,[a] Rajkumar Sunil Singh,[a] Naorem Shanta Singh *[b] and Ningombam Yaiphaba *[a]

Received 19th August 2024,
Accepted 24th October 2024

DOI: 10.1039/d4sd00277f

rsc.li/sensors

Ce^{3+}-sensitized Tb^{3+}-activated SrF_2 nanophosphors (NPs) were synthesized using the hydrothermal method. Crystallographic characterization using X-ray diffraction confirms the formation of cubic SrF_2 with space group $Fm\bar{3}m$ for all samples. The FESEM image indicates spherical-shaped particles. Surface functionalization renders that the NPs are dispersible in water. The strong green emission of SrF_2:5% Tb^{3+}, 5% Ce^{3+} at 541 nm increases by 50-fold than that of SrF_2:5% Tb^{3+}. The resonance energy transfer between Ce^{3+} and Tb^{3+} *via* multipolar interactions is observed. The energy transfer efficiency and spectral overlap integral are calculated. The absolute quantum yield of SrF_2:5% Tb^{3+}, 5% Ce^{3+} is observed to be ~12%. The NPs show excellent biocompatibility towards the HeLa cell line with 70% cell viability. Intercellular uptake of the SrF_2:5% Tb^{3+}, 5% Ce^{3+} nanophosphor is fair, and its potential for anti-counterfeiting and forensic fingerprint applications is observed.

1. Introduction

Recently, rare earth-doped luminescent inorganic materials have become promising in various applications, such as solid-state lighting, displays, photovoltaic devices, sensors, dental applications, biological labeling, security ink, *etc.*[1–7] The presence of well-shielded intra 4f–4f transitions in rare earth ions are responsible for their unique luminescence properties, such as sharp band emissions, long luminescence lifetime, and excellent stability, making them popular activators.[8–11] However, they encounter weak luminescence efficacy due to Laporte's forbidden transitions, limiting their applications. Increasing the luminescence efficacy by adopting methods like sensitization, charge compensation, core–shell formation, *etc.* has been reported by many researchers. Luo *et al.* reported enhanced luminescence due to efficient energy transfer from Ce^{3+} to Tb^{3+} in Ce^{3+} and Tb^{3+} co-doped glasses and glass ceramics containing SrF_2 nanocrystals.[12] Likewise, charge compensation and efficient energy transfer from Ce^{3+} to Tb^{3+} or Mn^{2+} in $Ca_9ZnLi(PO_4)_7$ have also been reported.[13,14] Similarly, the enhanced luminescence in the white region by the core–shell formation of the lanthanide-doped SrF_2 core and CaF_2 as the shell has been reported.[15] Amongst them, sensitization by choosing an appropriate sensitizer is an easier way to improve luminescence. For sensitization, Ce^{3+} ions are commonly used as a sensitizer for other rare-earth ions because they have emissions in the range of 300–360 nm, which overlaps with the excitation spectrum of the other rare-earth ions.[16,17] Tb^{3+} ions, which have an excitation wavelength in the range of 280–450 nm, correspond to the emissions of Ce^{3+} ions.[18] Thus, good energy transfer can occur easily from Ce^{3+} to Tb^{3+} ions, resulting in the enhancement of emission intensity, *i.e.*, Ce^{3+} ions can act as a sensitizer.

Alkaline earth fluorides of cubic type, especially CaF_2, SrF_2, and BaF_2, are excellent host materials for rare earth metal ions. This is due to their outstanding luminescence properties, such as low phonon energies, large band gaps, high stabilities, high ionicities, and ionic conductivities.[15–22] Many researchers have extensively studied fluoride phosphors because of their ease of synthesis and good luminescence. Zhang's group reported the mesoporous lanthanide doped SrF_2 for luminescence properties and field emission displays. They also reported the synthesis of monodisperse CaF_2:Ce^{3+}/Tb^{3+} hollow spheres as smart drug carriers.[23] Ansari *et al.* reported the synthesis of a highly stable water dispersion of CaF_2:Ce/Tb nanocrystals for optical band gap and photoluminescence properties.[24] Besides, many research groups have reported the structural, spectroscopic, and cytotoxicity studies of upconverting SrF_2 nanoparticles.[25–27] Yan *et al.* also reported the single phase SrF_2:Tb^{3+}, Eu^{3+} phosphors using the chemical co-precipitation method. They

[a] *Department of Chemistry, Manipur University, Imphal – 795003, India. E-mail: yaiphaba@manipuruniv.ac.in*
[b] *Department of Physics, School of Sciences, Nagaland University, Lumami-798627, India. E-mail: ssnaorem@nagalanduniversity.ac.in*

studied the high energy efficiency and multi-color emissions, which have potential applications in white light-emitting diodes.[28] Another author also reported the luminescent enhancement of Ce^{3+} and Tb^{3+} doped CaF_2 and they analyzed the effect of Li^+ ion co-doped in the nanoparticles and hyperthermia application of Ce^{3+} doped CaF_2/Fe_3O_4 nanocomposites.[20] Several applications, such as security inks and fingerprint detection of the upconverted nanophosphors, have been reported by many researchers.[29,30] Jin reported the Eu^{3+} doped BaF_2 and SrF_2 nanocrystals for luminescence properties and telecommunication.[31] An eco-friendly synthesis of SrF_2 nanoparticles and studies on the *in vitro* biocompatibility and antibacterial properties have been reported.[32] Eu-doped BaF_2 nanoparticles were used for bioimaging applications.[33] However, reports on multifunctional applications such as biocompatibility, security inks, and fingerprint detection of Ce^{3+} and Tb^{3+} co-doped SrF_2 are still rare.

In this present work, we have chosen SrF_2 as a host matrix, Tb^{3+} as the activator, and Ce^{3+} as the sensitizer for preparing single-phase multifunctional biocompatible luminescent NPs. SrF_2:Tb^{3+}, Ce^{3+} nanophosphors have been synthesized using trisodium citrate as a capping agent by a hydrothermal method. The crystal structure, morphology, luminescence properties, quantum yield and energy transfer mechanism were studied. Because of the potential biological applications of synthesized NPs, their cytotoxicity was assessed. The biocompatibility of the as-synthesized nanophosphors was performed on the HeLa cell line. Moreover, intracellular uptakes of our NPs were also analyzed using fluorescence microscopy. Furthermore, luminescence anti-counterfeiting and forensic fingerprint detection were also investigated.

2. Experimental sections

2.1. Reagents and materials

Strontium nitrate ($Sr(NO)_3$, Sisco-chem, 98.50%), purified ammonium fluoride (NH_4F, Merck), trisodium citrate dihydrate ($C_6H_5Na_3O_7{\cdot}2H_2O$, Himedia, 99.00%), terbium(III) nitrate pentahydrate ($Tb(NO)_3{\cdot}5H_2O$, Sigma-Aldrich, 99.90%), cerium(III) carbonate hydrate ($Ce_2(CO_3)_3{\cdot}xH_2O$, Sigma-Aldrich, 99.90%), ethylene glycol and deionized water were used in the synthesis of the materials. The regents were analytically pure and used without further purification.

2.2. Synthesis of $Sr_{0.90}F_2$:5% Tb^{3+}, 5% Ce^{3+} (SrF_2:5% Tb^{3+}, 5% Ce^{3+}) samples

In a typical synthesis of SrF_2:5% Tb^{3+}, 5% Ce^{3+} samples, first, a stoichiometric proportion of $Ce_2(CO_3)_3{\cdot}xH_2O$ (0.048 g) was dissolved in concentrated HNO_3 to obtain its nitrate, and the excess acid was removed by the addition of water, followed by evaporation to dryness. Then, it was dissolved together with a stoichiometric proportion of $Sr(NO)_3$ (0.676 g) and in 20 mL of 1 : 1 ethylene glycol and water solution. 20 mL of 1 : 1 ethylene glycol and aqueous solution of 0.595 g NH_4F were added and stirred vigorously for 30 min. Thereafter, 20 mL of 1 : 1 ethylene glycol, an aqueous solution of 0.089 g $Tb(NO)_3{\cdot}5H_2O$, 20 mL of 1 : 1 ethylene glycol and an aqueous solution of 1.176 g $C_6H_5Na_3O_7{\cdot}2H_2O$ were added. The whole mixture was stirred for another 30 minutes and then transferred to a Teflon-lined autoclave. The vessel was kept in a preheated oven at 140 °C for 2 hours, after which it was removed and cooled to room temperature. The product was collected by centrifugation and washed with deionized water and acetone. Finally, the product was dried at 40 °C for further analysis.

2.3. Cell viability studies: MTT assay

The National Centre for Cell Science (NCCS) in Pune provided the HeLa cancer cell line. The cells were grown in DMEM (Dulbecco's modified Eagle medium) medium containing 10% FBS and 0.1% penicillin–streptomycin at 37 °C in a humidified atmosphere containing 5% CO_2. The biocompatibility and cytotoxicity of nanocomposites were assessed using the MTT {3-(4,5-dimethylthiazol-2-yl)-2,5-diphenyltetrazolium bromide} reduction assay.[34] After 48 h of treatment, 15 μL of MTT solution (5 mg mL^{-1}) was added to each well (96 well plate) and incubated for 3 h. During this time, the developed formazan crystals were dissolved by adding 100 μL of DMSO to each well, and absorbance was measured at 570 nm using a Varioskan™ LUX multimode microplate reader.[35] Cell viability was calculated as: $[A_{570}$(treated cells) − background$]/[A_{570}$(untreated cells) − background$]$ × 100. Studies were performed in triplicate for each data point.

2.4. Intracellular uptake studies

HeLa cells (5×10^4) were seeded on coverslips placed in the wells of a 6-well plate and treated with different concentrations of NPs for 24 h. The cells were washed with PBS twice, permeabilized with 0.1% Triton X100 for 5 min, and washed with PBS twice. The cells were fixed with 4% paraformaldehyde for 10 min and washed with PBS twice. The fixed cells were stained with DAPI (4,6-diamidino-2-phenylindole) for 5 min in the dark and washed with PBS twice.[36] The intracellular uptake imaging of the NPs in HeLa cell lines was performed using fluorescence microscopy.

2.5. Characterization

Powder XRD was carried out on the samples using a PANalytical X-ray diffractometer (X'Pert Pro) Cu (Kα) radiation (λ = 1.5405 Å), 2θ range of 15–90° to determine the identification and purity of the phase. The morphology and size of the synthesized phosphors were observed by FE-SEM (JEOL, JSM 6390LV). An energy dispersive X-ray spectroscopy (EDS/EDX) attached to a Quanta − 250 SEM was used to analyze the elemental composition. The absorption spectra were recorded using a UV-vis spectrophotometer (UV-2600, Shimadzu). Shimadzu IRAffinity 1S was used to record the Fourier transform infrared (FT-IR) spectra. The photoluminescence spectra and their decay

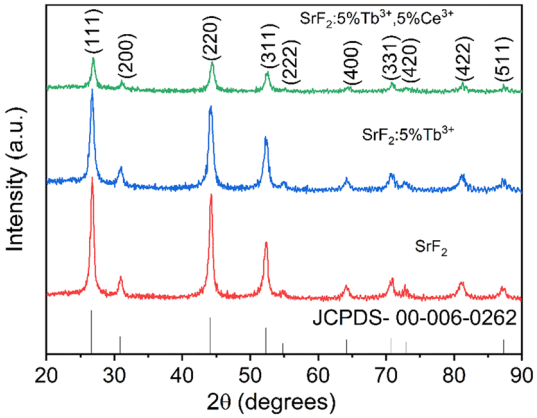

Fig. 1 XRD pattern of SrF_2, SrF_2:5% Tb^{3+}, and SrF_2:5% Tb^{3+}, 5% Ce^{3+} nanophosphors.

as well as quantum yield (QY) were measured with a Horiba make Fluoromax-4CP spectrofluorometer equipped with an arc xenon lamp 150 W and 5 W microsecond pulse lamp. The QY was measured by integrating the sphere K-sphere 'petite' (Photon Technology International). All the measurements were done in the emission mode. The absolute QY was calculated using the relation, $\Phi\,(\%) = \dfrac{\int I_{\text{emission}}\,d\lambda}{\int I_{\text{sample holder}}\,d\lambda - \int I_{\text{sample}}\,d\lambda}$ where I_{emission} = luminescence emission intensity of the sample, $I_{\text{sample holder}}$ = the intensity of excitation light only the quartz slide and I_{sample} = the intensity of the light used for exciting the sample placed on the quartz slide. The difference in the denominator gives the photons absorbed by the sample. All the PL measurements were carried out on the glass (for PL and decay lifetime) and quartz slides (for QY) at room temperature. The luminescence decay lifetime for Ce^{3+} emission was measured by the TCSPC technique with Horiba make DeltaFlex having pulse LED laser 295 ± 10 nm as source (pulse width ≤1.2 ns).

3. Results and discussions

3.1. XRD studies

Fig. 1 shows the X-ray diffraction patterns of SrF_2, SrF_2:5% Tb^{3+}, SrF_2:5% Tb^{3+}, 5% Ce^{3+} nanophosphors. The diffraction patterns can be indexed to the standard diffraction data 00-006-0262 for the cubic phase of SrF_2 possessing the $Fm\bar{3}m$ space group. No additional phases, such as Tb_2O_3, Ce_2O_3, Ce_3O_4, *etc.*, are observed upon adding Tb^{3+} and Ce^{3+} ions into the SrF_2 lattice. The calculated lattice parameters, crystallite sizes, and unit cell volumes are shown in Table 1. The crystallite sizes were calculated using the Scherrer formula: $d = k\lambda/\beta\cos\theta$. The strongest peak corresponding to the (111) plane was used to calculate the average crystallite size of the samples. Again, using the Williamson–Hall model, the crystallite sizes were also calculated, which were almost similar to those calculated using the Scherrer formula. From Table 1, it is observed that the unit cell volume is increased on Tb^{3+} substitution, whereas the ionic radius of the Sr^{2+} ion (1.32 Å) is larger than that of Tb^{3+} (0.92 Å) at coordination number 6.[37] Our result is contradictory to the Vegard's law; the unit cell volume must be slightly decreased as compared to that of pure SrF_2. This is due to the occupancy of the excess fluoride ions in the interstitial sites, which compensate for the excess positive charge due to the substitution of trivalent lanthanide ions at Sr^{2+} sites. The balanced chemical equation can be represented as $2Sr^{2+} \rightarrow Ln^{3+} + F^-$. It may also be due to the formation of tetragonal (C_{4v}) or trigonal (C_{3v}) and electronic repulsions between F^- ions, which leads to the expansion of unit cell volume.[38,39] However, a small increase in the unit cell volume is observed for Ce^{3+} and Tb^{3+} co-doped SrF_2 NPs, which is due to the ionic radius of Ce^{3+} (1.01 Å) ion being greater than that of Tb^{3+} ion (0.92 Å) at coordination number 6.[37,40]

3.2. FESEM and EDS studies

The morphologies of the SrF_2:5% Tb^{3+}, 5% Ce^{3+} nanophosphors were studied by FESEM imaging, as shown in Fig. 2(a). The FESEM image shows the formation of spherical-shaped nanoparticles with a particle size range of 50–60 nm. Fig. 2(b) shows the typical histogram of the particle diameter (size) for the sample SrF_2:5% Tb^{3+}, 5% Ce^{3+}. The energy dispersive spectra of SrF_2, SrF_2:5% Tb^{3+}, SrF_2:5% Ce^{3+}, and SrF_2:5% Tb^{3+}, 5% Ce^{3+} nanophosphors, respectively, are shown in Fig. 2(c–f). The Sr, F, Ce, and Tb elements are detected from the respective nanophosphor samples, indicating the successful preparation of Tb^{3+} and Ce^{3+} co-doped SrF_2 NP.

3.3. FT-IR studies

Fig. 3 shows the FT-IR spectrum of the as-prepared SrF_2:5% Tb^{3+}, 5% Ce^{3+} nanophosphors. The strong single broad peak at around 3600–3300 cm^{-1} corresponds to the O–H bond stretching vibration of the ethylene glycol/H_2O used as a solvent. The peaks at 1069–1252 cm^{-1} correspond to the CH_2 bending from ethylene glycol.[41] Other bands at 1401 and 1575 cm^{-1} arise from the symmetric and asymmetric vibrations of COO^- from the capping agent added during the synthesis, which gets adsorbed on the surface of the particles.[42] The band at 460

Table 1 Lattice parameters and crystallite sizes of SrF_2, SrF_2:5% Tb^{3+}, and SrF_2:5% Tb^{3+}, 5% Ce^{3+} nanophosphors

Sample	Lattice parameter a (Å)	Unit cell volume (Å^3)	Crystallite size (nm)	
			Debye	Williamson
Reference JCPDS 00-006-0262 SrF_2	5.80	195.11		
SrF_2	5.76	191.76	10	12
SrF_2:5% Tb^{3+}	5.77	192.19	8	9
SrF_2:5% Tb^{3+}, 5% Ce^{3+}	5.78	193.58	7	8

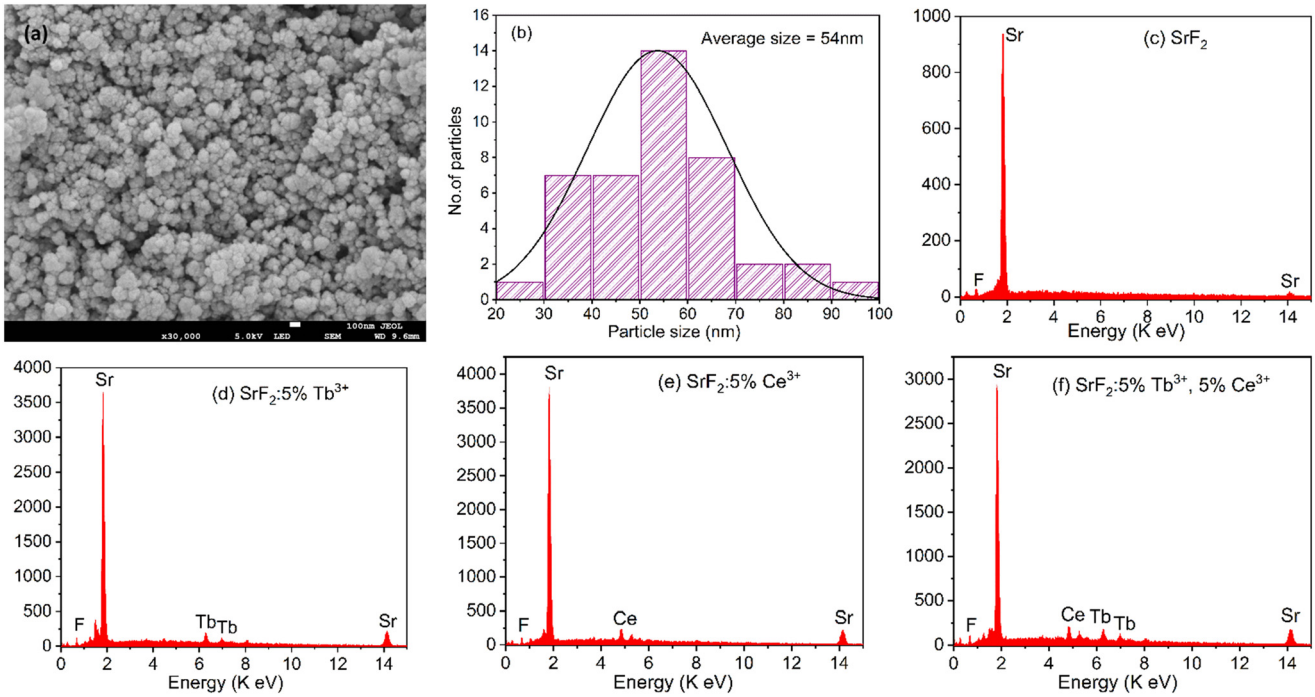

Fig. 2 (a) FESEM image, (b) histogram of the particle diameters, and (c)–(f) energy dispersive spectrum (EDS) of SrF_2, SrF_2:5% Tb^{3+}, SrF_2:5% Ce^{3+} and SrF_2:5% Tb^{3+}, 5% Ce^{3+} nanophosphors.

cm^{-1} is assigned to the Sr–F stretching vibration. The presence of ethylene glycol and trisodium citrate dihydrate, along with the NPs, will help in the incorporation/dispersion of NPs in polar media and thin films.

3.4. Optical studies

The absorption spectra of the as-synthesized SrF_2, SrF_2:5% Tb^{3+}, and SrF_2:5% Tb^{3+}, 5% Ce^{3+} nanophosphors are shown in Fig. 4. The NPs show a strong absorption in the UV spectral region of 200–400 nm. It is observed that there is a peak at around 235 to 256 nm, with the maximum at 245 nm in Tb^{3+} doped SrF_2 NPs. On the other hand, for Ce^{3+} co-doped Tb^{3+} doped SrF_2 NPs, in addition to the above peak, there is another peak at 281 to 306 nm with the maximum at 293 nm. Since the optical bandgap of SrF_2 is ~11 eV,[43] the absorption band lies in the vacuum UV region, which is beyond our spectrophotometer detection capability. Therefore, the corresponding absorption bands observed in the region above may be related to the defect states localized in the forbidden region of SrF_2. Researchers have already reported similar studies on unactivated CaF_2, SrF_2, BaF_2 and lanthanide-activated CaF_2.[44,45] As Mukherjee *et al.* have reported in the lanthanide-activated CaF_2,[44] these defect states may arise from the creation of vacancies to maintain charge neutrality during the substitution of Sr^{2+} sites by Ce^{3+}

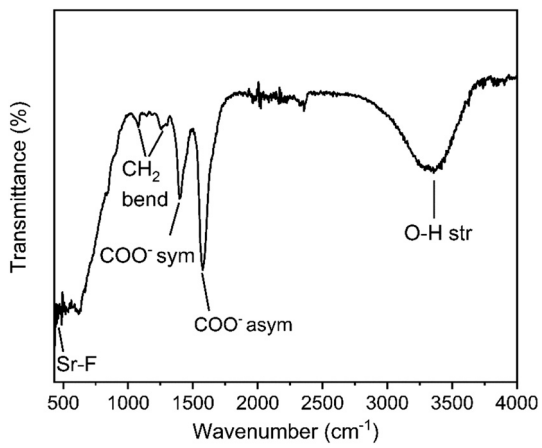

Fig. 3 FT-IR spectrum of SrF_2:5% Tb^{3+}, 5% Ce^{3+} nanophosphors.

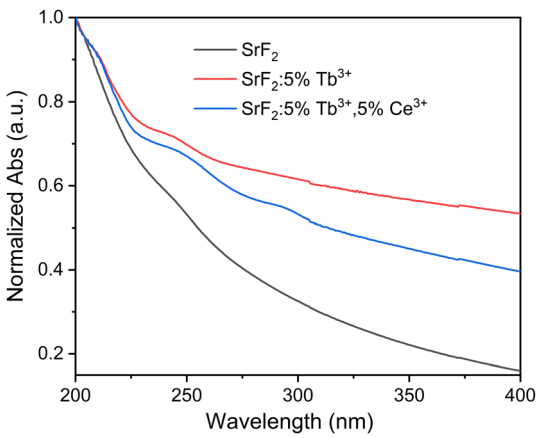

Fig. 4 UV-vis spectra of SrF_2, SrF_2:5% Tb^{3+}, and SrF_2:5% Tb^{3+}, 5% Ce^{3+} nanophosphors.

and/or Tb^{3+}. Also, F-interstitial sites may act as defect sites during lanthanide substitution for charge compensation (as the F^- source was taken 2 times its molar requirement).

3.5. Photoluminescence (PL) studies

PL excitation spectra of SrF_2:5% Ce^{3+}, SrF_2:5% Tb^{3+} and SrF_2:5% Tb^{3+}, 5% Ce^{3+} nanophosphors monitored at the emission wavelengths at 330 nm (for SrF_2:5% Ce^{3+}) and 541 nm for the remaining 2 (two) are displayed in Fig. 5(a). The excitation spectrum of SrF_2:5% Ce^{3+} consists of two broad excitation bands in the range of 230 to 320 nm, with the maximum peaks at 260 and 297 nm, corresponding to the spin-allowed 4f–5d transitions of Ce^{3+} ions. These are originated from the transitions of $^2F_{5/2}$ and $^2F_{7/2}$ ground states to the $^2D_{3/2}$ and $^2D_{5/2}$ excited states of 5d orbitals.[46] Though, the excitation spectrum of SrF_2:5% Tb^{3+} shows a broad peak at 250–260 nm, which corresponds to the 4f–5d and Tb–O charge transfer.[8] In addition, the excitation peaks observed in the longer wavelength region at 349 ($^7F_6 \rightarrow {}^5D_1$), 355 ($^7F_6 \rightarrow {}^5D_1$), 363 ($^7F_6 \rightarrow {}^5D_1$) and 370 ($^7F_6 \rightarrow {}^5D_1$) nm are associated with the 4f–4f transitions of Tb^{3+} ions from the $^7F_6$ ground state to the different higher excited states. Meanwhile, the SrF_2:5% Tb^{3+}, 5% Ce^{3+} sample shows two main absorption peaks at 260 and 297 nm. These peaks are related to the spin-allowed 4f–5d transitions of Ce^{3+} (as discussed above). Here, the 4f–5d transition and/or Tb–O charge transfer band of Tb^{3+} is not seen, as it might have merged with the 260 nm excitation peak due to Ce^{3+}. The excitation peaks are also observed in the longer wavelength region due to absorption within the Tb^{3+} ions (as discussed above). The strong excitation peak at 260 and 297 nm related to Ce^{3+} indicates the strong energy transfer from Ce^{3+} to the excited states of Tb^{3+}. Fig. 5(b) shows the normalized excitation spectra of SrF_2:5% Ce^{3+}, SrF_2:5% Tb^{3+} and SrF_2:5% Tb^{3+}, 5% Ce^{3+} at different emission peaks related to their characteristic emissions, *i.e.*, 330 nm for Ce^{3+} and 488 ($^5D_4 \rightarrow {}^7F_6$), 541 ($^5D_4 \rightarrow {}^7F_5$), 583 ($^5D_4 \rightarrow {}^7F_4$) and 620 ($^5D_4 \rightarrow {}^7F_3$) nm of Tb^{3+} to check any additional peaks, which can be correlated to the Ce^{3+} (sensitizer/donor) emission. Here, it is observed that excitation bands related to the Ce^{3+} emission are observed only in SrF_2:5% Ce^{3+} and SrF_2:5% Tb^{3+}, 5% Ce^{3+}. Such a band is not observed in SrF_2:5% Tb^{3+}.

The PL emission spectra of SrF_2:5% Ce^{3+}, SrF_2:5% Tb^{3+} and SrF_2:5% Tb^{3+}, 5% Ce^{3+} nanophosphors under different excitation wavelengths are shown in Fig. 6(a). For SrF_2:5% Ce^{3+}, the excitation wavelengths are 260 and 297 nm. Both spectra show the characteristic emission of Ce^{3+} in the range of 300–400 nm with a maximum at 330 nm. This is due to the transition from the excited d-level to the f-level ground state of Ce^{3+}. On the other hand, excitation wavelengths for SrF_2:5% Tb^{3+} are related to the Tb^{3+} absorption at 255 and 370 nm. The characteristic emission peaks of Tb^{3+} are seen at 488 ($^5D_4 \rightarrow {}^7F_6$), 541 ($^5D_4 \rightarrow {}^7F_5$), 583 ($^5D_4 \rightarrow {}^7F_4$) and 620 ($^5D_4 \rightarrow {}^7F_3$) nm. Meanwhile, the emission spectra for SrF_2:5% Tb^{3+}, 5% Ce^{3+} were recorded under the excitation of 260, 297, and 370 nm. Here, all the emissions related to Ce^{3+} and Tb^{3+} are observed. However, the Ce^{3+} emission intensity is drastically reduced compared to SrF_2:5% Ce^{3+}, while the Tb^{3+}-related emission peaks are enhanced when compared to SrF_2:5% Tb^{3+}. Thus, it suggests the efficient energy transfer from the Ce^{3+} excited states to the excited states of Tb^{3+} ions (discussed later).[47] The emission peak corresponding to $^5D_4 \rightarrow {}^7F_5$ at 541 nm is dominant over others; therefore, the overall emission color is green. The emission intensity of SrF_2:5% Tb^{3+}, 5% Ce^{3+} is found to be enhanced ~50 times than that of SrF_2:5% Tb^{3+} under similar radiation exposure.

According to Dexter's theory,[48] the spectral overlap between the excitation spectrum of the activator and the emission spectrum of the sensitizer is required to support the energy transfer from sensitizer to the activator. Therefore, we demonstrated the normalized spectral overlap between the SrF_2:5% Tb^{3+} excitation and SrF_2:5% Ce^{3+} emission, as shown in Fig. 6(b). A broad spectral overlap between these two spectra in the wavelength ranges from 300 to 450 nm, indicating the occurrence of efficient energy transfer from

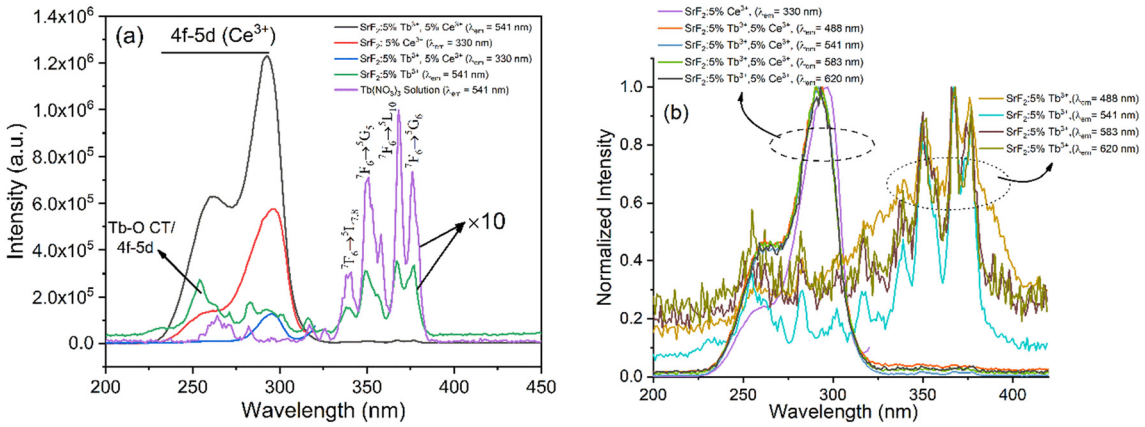

Fig. 5 (a) Excitation spectra of SrF_2:5% Tb^{3+}, SrF_2:5% Ce^{3+} and SrF_2:5% Tb^{3+}, 5% Ce^{3+} (b) normalized excitation spectra of SrF_2:5% Tb^{3+}, SrF_2:5% Ce^{3+} and SrF_2:5% Tb^{3+}, 5% Ce^{3+} samples at all the emission peaks.

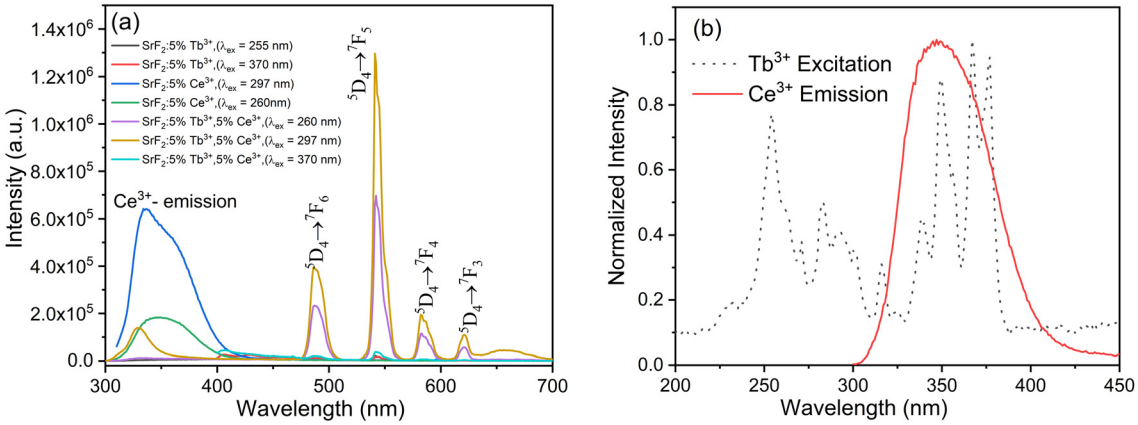

Fig. 6 (a) Emission spectra of SrF_2:5% Tb^{3+}, SrF_2:5% Ce^{3+} and SrF_2:5% Tb^{3+}, 5% Ce^{3+} nanophosphors and (b) normalized spectral overlap of SrF_2:5% Ce^{3+} emission and SrF_2:5% Tb^{3+} excitation.

Ce^{3+} to Tb^{3+} ions in SrF_2:5% Tb^{3+}, 5 Ce^{3+}.[49,50] The probable energy transfer mechanism is shown in Fig. 7. The sensitization of Tb^{3+} by Ce^{3+} in SrF_2 may also occur *via* a charge trap-mediated process. Such an energy transfer process was illustrated by Mukherjee *et al.* in Tb^{3+}/Eu^{3+} co-doped CaF_2.[44] Here, the sensitization of Tb^{3+} by Ce^{3+} in SrF_2 may also occur *via* a charge trap-mediated process where the photogenerated electron from the initially excited Ce^{3+} energy level recombines with a photogenerated hole at the Tb^{3+} center and thus populates the Tb^{3+} luminescent energy level $^5D_4$. Later, the radiative transition occurs from the excited state $^5D_4$ to the ground states with enhanced emission.

The PL decay lifetime curves of the SrF_2:5% Ce^{3+} and SrF_2:5% Tb^{3+}, 5% Ce^{3+} samples at 295 ± 10 nm excitation when the emission is monitored at 330 nm along with the instrument response function (IRF) are shown in Fig. 8(a). The decay lifetime values of SrF_2:5% Ce^{3+}, SrF_2:5% Tb^{3+}, 5% Ce^{3+} samples were calculated using eqn (1)

$$I(t) = I_0 \exp(-t/\tau) \quad (1)$$

The decay lifetimes are found to be ~15.35 and 7.82 ns, respectively, whereas the value of IRF is ~1.7 ns. The typical curve fitting using eqn (1) is shown in Fig. 8(b). The PL decay lifetime of Ce^{3+} is decreased in the presence of Tb^{3+}. This is due to the non-radiative excited electron transfer from the excited states of Ce^{3+} to the excited states of Tb^{3+} at the expense of radiative transition to the ground state within Ce^{3+}. Thus, this establishes the occurrence of energy transfer from Ce^{3+} to Tb^{3+}. Further, this corroborates the existence of energy transfer discussed in steady-state PL studies. The energy transfer efficiency (φ) was calculated from the lifetime values using[51]

$$\varphi = 1 - \frac{\tau_S}{\tau_{SO}} \quad (2)$$

where τ_S and τ_{SO} are the lifetimes of Ce^{3+} in the presence and absence of Tb^{3+}, respectively. The φ is found to be 49%. Fig. 9(a and b) shows the PL decay curves of the $^5D_4$ level of Tb^{3+} for the SrF_2:5% Tb^{3+} and SrF_2:5% Tb^{3+}, 5% Ce^{3+} at 370 nm excitation when the emission is monitored at 541 nm. Fig. 9(c) shows the decay curve of the SrF_2:5% Tb^{3+}, 5% Ce^{3+} sample at 297 nm excitation when the emission is monitored at 541 nm. The following decay equation was used to calculate the PL decay lifetime:[51]

$$I = I_o \exp\left(-\frac{t}{\tau}\right) - \left(2bt^{\frac{1}{2}}\right) \quad (3)$$

Here, I and I_o represent the emission intensities at a given time, 't' and t = 0, respectively, and 'b' is the quencher concentration dependent on diffusion co-efficient, while the power of 't' is taken $\frac{1}{2}$ as the energy transfer is assumed to be resonance type. 'τ' is the PL decay lifetime. The PL decay lifetime values of the SrF_2:5% Tb^{3+} and SrF_2:5% Tb^{3+}, 5% Ce^{3+} samples at 370 nm excitation when the emission is monitored at 541 nm were found to be 4.10 and 4.56 ms, respectively. The lifetime values of the SrF_2:5% Tb^{3+}, 5% Ce^{3+} samples at 297 nm excitation when the emission is monitored at 541 nm was found to be ~6 ms.

Generally, the energy transfer between Ce^{3+} and Tb^{3+} is possible *via* two mechanisms: exchange interaction and multipolar interaction. The distance between the donor and the acceptor plays an important role in determining the probable type of energy transfer. This can be checked by

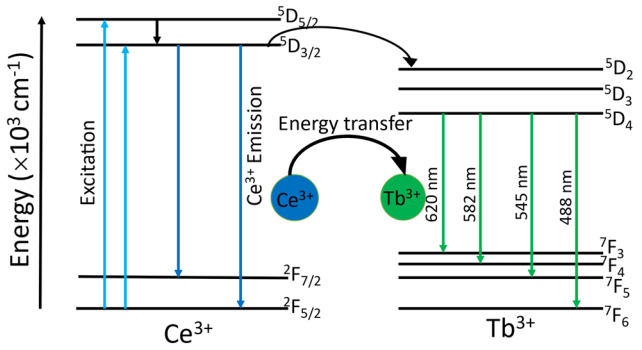

Fig. 7 Schematic energy transfer pathways from Ce^{3+} to Tb^{3+}.

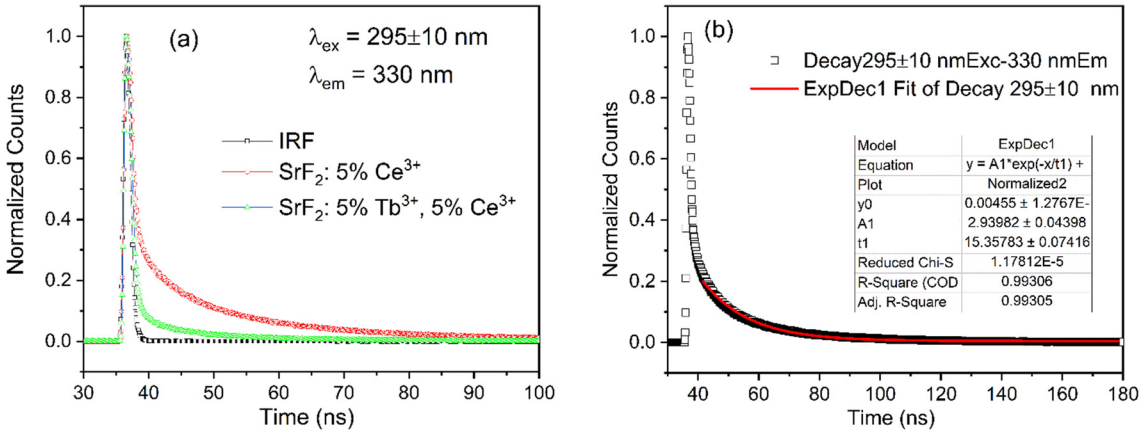

Fig. 8 (a) Decay profile of IRF, SrF_2:5% Ce^{3+} and SrF_2:5% Tb^{3+}, 5% Ce^{3+} samples excited at 295 ± 10 nm and emission is monitored at 330 nm, (b) decay profile of SrF_2:5% Ce^{3+} nanophosphors excited at 295 ± 10 nm and emission is monitored at 330 nm.

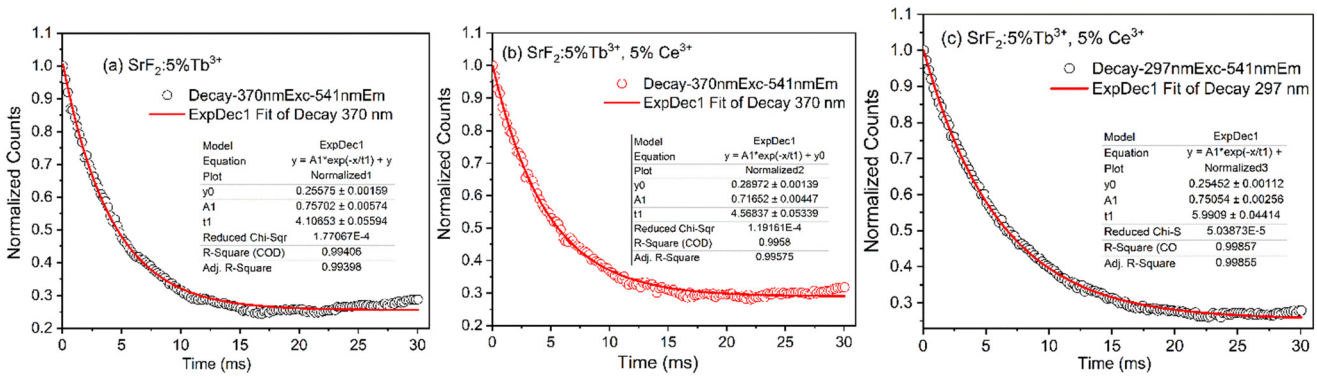

Fig. 9 (a and b) Decay profile of SrF_2:5% Tb^{3+} and SrF_2:5% Tb^{3+}, 5% Ce^{3+} nanophosphors excited at 370 nm and emission is monitored at 541 nm and (c) decay profile of SrF_2:5% Tb^{3+}, 5% Ce^{3+} samples excited at 297 nm and emission is monitored at 541 nm.

calculating the critical distance (R_c) between Tb^{3+} and Ce^{3+} ions, using the following equation,[52,53]

$$R_c = 2\left(\frac{3V}{4\pi X_c N}\right)^{1/3} \quad (4)$$

where V represents the unit cell volume, X_c is the concentration and N is the number of the cations at the center of the unit cell in the host. In the SrF_2 host lattice, the unit cell volume is 193.58 Å^3, the total concentration is 10% and the value of N is 4. The calculated value of R_c using eqn (4) is found to be 9.7 Å, which is larger than 5 Å. This indicates the energy transfer mechanism from Ce^{3+} to the excited state of Tb^{3+} in the SrF_2 is dominated by multipolar interactions; thereby, the exchange interaction type of energy transfer can be ignored.[53]

To further elucidate the resonance energy transfer, the overlap spectral integral ($J(\lambda)$), which is the expression of the degree of spectral overlap between the donor emission and the acceptor absorption, can be calculated as[51]

$$J(\lambda) = \int_0^\infty F_D(\lambda)\varepsilon_A(\lambda)\lambda^4 d\lambda = \frac{\int_0^\infty F_D(\lambda)\varepsilon_A(\lambda)\lambda^4 d\lambda}{\int_0^\infty F_D(\lambda) d\lambda} \quad (5)$$

$F_D(\lambda)$ is the luminescence intensity of the donor and is dimensionlesss. $\varepsilon_A(\lambda)$ is the molar extinction coefficient of the acceptor in M^{-1} cm^{-1}, and λ is expressed in nanometre. According to Förster's resonance energy transfer theory, the energy transfer efficiency (φ) is dependent on the distance between the donor and acceptor (R_c),[51]

$$\varphi = \frac{{R_0}^6}{{R_0}^6 + {R_c}^6} \quad (6)$$

where R_0 is the Förster critical distance, which is defined as the distance for φ to be 50%. Using eqn (6) and with the obtained φ = 49% and R_c = 9.7 Å, the R_0 is calculated to be 9.8 Å. Again, R_0 can be further defined as follows:[51]

$${R_0}^6 = 8.79 \times 10^{-5} (\kappa^2 n^{-4} \eta_D J(\lambda)) \quad (7)$$

where 'n' is the refractive index of the medium (here, SrF_2), κ^2 is the relative dipole orientation in the space of the transition dipoles of the donor and acceptor and is usually assumed to be $\frac{2}{3}$. η_D is the quantum yield of the donor in the absence of the acceptor. The spectral integral ($J(\lambda)$) is expressed in M^{-1} cm^{-1} nm^4. Using eqn (7) and taking 'n' =

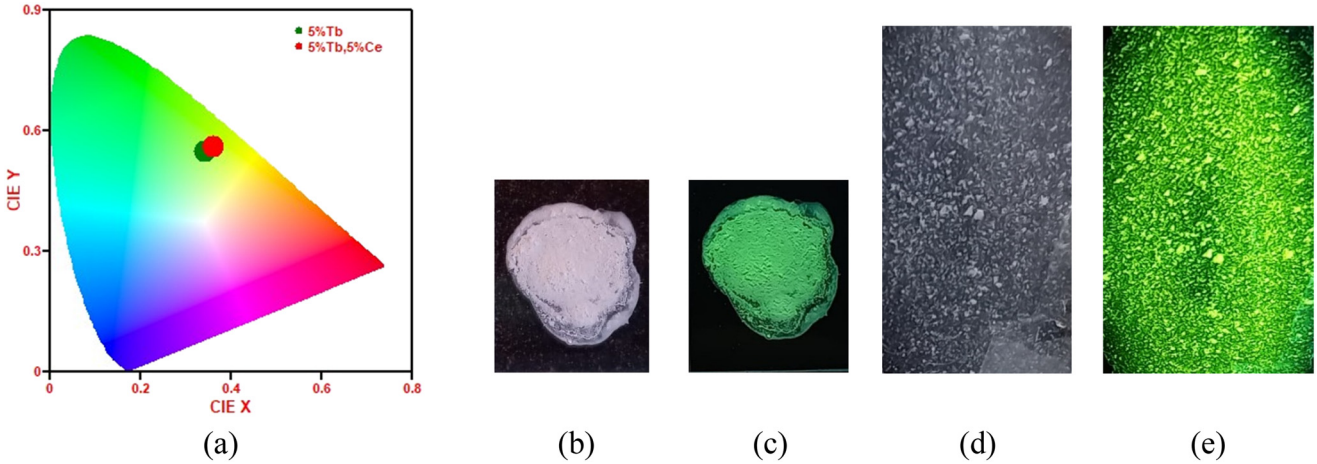

Fig. 10 (a) CIE chromaticity diagram of SrF_2:5% Tb^{3+} and SrF_2:5% Tb^{3+}, 5% Ce^{3+} nanophosphors excited at 255 nm. (b) and (d) Before exposure and (c) and (e) after exposure of powder and a thin film of the SrF_2:5% Tb^{3+}, 5% Ce^{3+} nanophosphors, respectively.

1.48 and η_D = 22% (given in the next paragraph), $J(\lambda)$ is calculated to 1.05×10^{10} M^{-1} cm^{-1} nm^4. It is also stated that if $0.5R_0 < R_c < 2R_0$, efficient energy transfer occurs.[53b]

3.6. CIE chromaticity coordinates and quantum yield efficiency

The calculated CIE coordinates diagram of SrF_2:5% Tb^{3+} and SrF_2:5% Tb^{3+}, 5% Ce^{3+} nanophosphors excited at 255 nm are shown in Fig. 10(a). The corresponding chromaticity coordinates for SrF_2:5% Tb^{3+} and SrF_2:5% Tb^{3+}, 5% Ce^{3+} nanophosphors, respectively, are (x = 0.34, y = 0.55) and (x = 0.36, y = 0.56). It can be seen that the emission of Tb^{3+} ions and Ce^{3+} ions co-doped SrF_2 nanophosphors corresponds to the green color. Moreover, as the Ce^{3+} ions co-doped into the Tb^{3+} ions doped SrF_2 nano-phosphor, the intensity of emission change is observed while the luminescence color is hardly changed. Fig. 10(b and c) shows the powder photographic image of the SrF_2:5% Tb^{3+}, 3% Ce^{3+} phosphor before and after 254 nm UV irradiation, suggesting the bright green color as suggested from the CIE diagram. We also prepared a thin film of the SrF_2:5% Tb^{3+}, 3% Ce^{3+} phosphor by using 5 mg of 10% PVA and borax solution. The physical photographic image of a thin film is shown in Fig. 10(d and e). The colour correlated temperature (CCT) was calculated by using the following equation:[54]

$$CCT = -437n^3 + 3601n^2 - 6861n + 5517$$

and

$$n = (x - 0.3320)/(0.1858 - y) \quad (8)$$

where x and y are the color coordinates.

The CCT values are found to be 5368 and 5023 for the SrF_2:5% Tb^{3+} and SrF_2:5% Tb^{3+}, 5% Ce^{3+} nanophosphors, and the values lie in the cold white region. Therefore, the as-prepared samples have a potential application in WLEDs. The absolute method was used to measure the quantum yield efficiency of the SrF_2:5% Tb^{3+}, 5% Ce^{3+} and SrF_2:5% Ce^{3+} phosphor using an integrating sphere. The value is found to be ~12% and 22%, respectively. Fig. 11(a and b) shows the quantum yield values of SrF_2:5% Tb^{3+}, 5% Ce^{3+} and SrF_2:5% Ce^{3+} nanophosphors from the instrument, respectively.

3.7. Cell viability studies: MTT assay

The cell viability of the SrF_2:5% Tb^{3+}, 5% Ce^{3+} nano-phosphor was carried out using HeLa cells by the MTT assay method as shown in Fig. 12. Different concentrations (6–200 μg mL^{-1}) of the nanophosphors were added to the cells and incubated for 24 h. At lower concentrations (6–25 μg mL^{-1}), >70% of cells were viable, while at higher concentrations

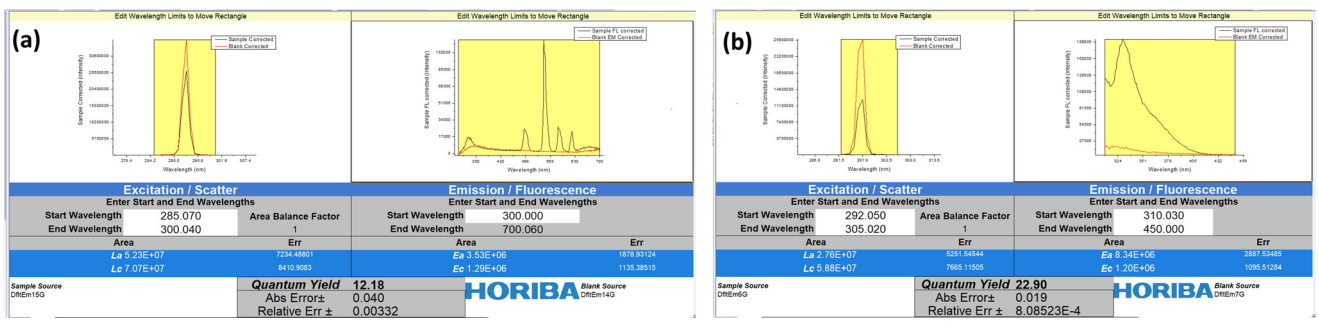

Fig. 11 Calculation of quantum yield for (a) SrF_2:5% Tb^{3+}, 5% Ce^{3+} and (b) SrF_2:5% Ce^{3+} nanophosphors using FluorEssence™ software in Horiba Fluoromax-4CP spectrofluorometer.

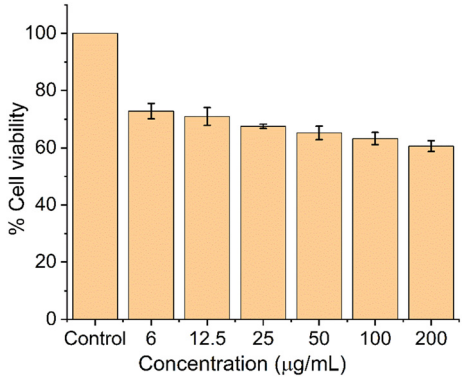

Fig. 12 Cell viability studies using HeLa cells at various SrF_2:5% Tb^{3+}, 5% Ce^{3+} nano-phosphor concentrations.

(50–200 μg mL^{-1}), >65% viability was observed. These data suggest the as-prepared nanophosphors displayed good cell viability over a wide concentration range.

3.8. Intracellular uptake studies in HeLa cells by fluorescence microscopy

Since SrF_2:5% Tb^{3+}, 5% Ce^{3+} nano-phosphor showed good biocompatibility towards HeLa cells, we decided to investigate the cellular uptake studies of the as-prepared nano-phosphor. Fig. 13 shows the intracellular uptake of the samples (100, 200, and 300 μg mL^{-1} concentrations) in HeLa cells after a 24-hour incubation period. Fluorescence microscopy was used to track the cellular uptake and internalization of the phosphor samples. The nuclei of the cells were counterstained with the DAPI dye (blue color) to help mark the locations of the cells under fluorescence microscopy. The green fluorescence from the sample-treated cell indicated the incorporation of the samples into HeLa cells. We also note that the blue and green colors are co-localized, which clearly shows that most of the phosphor samples internalize into the nuclei of the cells and not the cytosol. The intensity of the green fluorescence increased with increasing concentration of the phosphor samples, indicating a concentration-dependent nuclear accumulation. This study demonstrated that cultured cells easily internalize phosphor samples, predominantly into the nuclei.

3.9. Applications for fingerprint detection and security ink

In addition to a high intracellular image, practical use of the visible fingerprint image of the SrF_2:5% Tb^{3+}, 5% Ce^{3+} phosphor was also carried out. Nowadays, fingerprint detection is the most important evidence in any criminal investigation. In this paper, we use the SrF_2:5% Tb^{3+}, 5% Ce^{3+} nano-phosphor for fingerprint detection on a glass slide, which is shown in Fig. 14(a and b). The powder sample was sprinkled on the surface of the glass slide and wiped out softly. The image was recorded under the 254 nm UV light. The fingerprint image of the sample before and after the irradiation of 254 nm UV light can be easily recognized by the naked eye, suggesting the as-prepared phosphor can have a potential application in forensic science.

Moreover, the as-prepared phosphor was also demonstrated in the security ink for an anti-counterfeiting application. The rare-earth-doped particles show visible emissions, thus, they have received attention for anti-counterfeiting applications. The invisible ink was prepared by dispersing 10 mg of the as-prepared phosphor in 2 mL of 10% PVA solution. The mixed solution was sonicated in an ultrasonic bath for 30 minutes to obtain a homogeneous dispersion. Then, a few words like MU were written with this ink, as shown in Fig. 14(c and d). Under daylight, the sample containing ink was invisible (Fig. 14c). But the green-colored MU patterns (Fig. 14d) can be observed under the irradiation of 254 nm UV light, indicating the as-prepared phosphor is highly compatible with anti-counterfeiting performance.

4. Conclusions

In conclusion, we have reported the synthesis and characterization, including biocompatibility studies of SrF_2: Tb^{3+}, Ce^{3+} nanophosphors. XRD patterns show the formation of the cubic phase of SrF_2 NPs. A small increase in the unit cell volume is observed with Ce^{3+} and Tb^{3+} co-doping due to excess fluoride ions in the interstitial sites of the host matrix. FESEM micrographs show the formation of spherical-shaped NPs. From FTIR, it is concluded that the capping agent, *i.e.*, trisodium citrate, is present in the as-prepared NPs. A defect-generated broad absorption is observed with good dispersibility in the optical studies. The phosphors show a strong green emission at 541 nm upon excitation at 297 nm, which is due to efficient

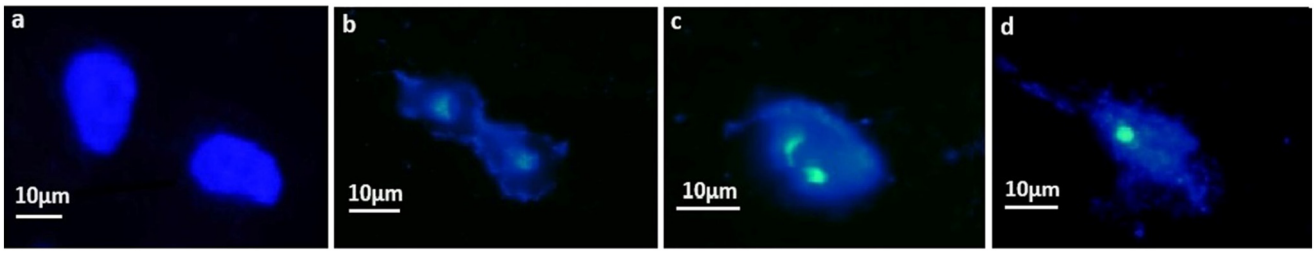

Fig. 13 Fluorescence microscopy imaging of HeLa cells after a 24 h incubation with varying concentrations of phosphor samples. (a) Untreated cells, (b) 100 μg mL^{-1}, (c) 200 μg mL^{-1}, and (d) 300 μg mL^{-1} of SrF_2:5% Tb^{3+}, 5% Ce^{3+} nano-phosphor. The nuclei are stained with DAPI (blue), while the phosphor samples exhibited green color.

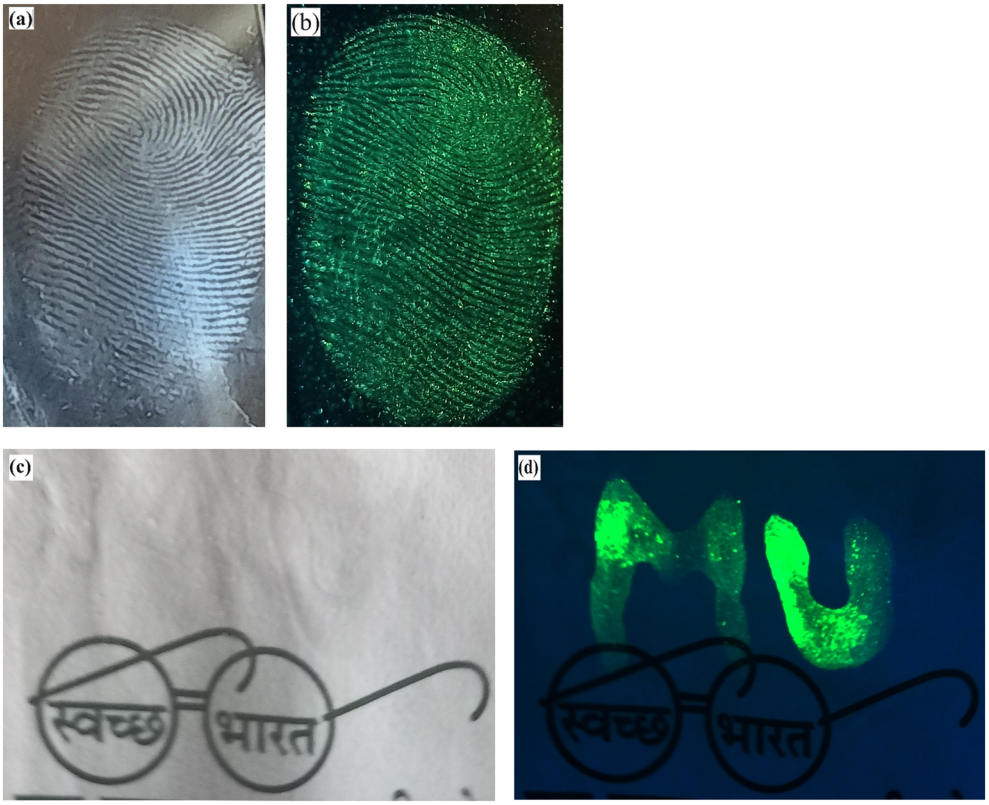

Fig. 14 Demonstration of fingerprint detection on (a and b) glass slide and (c and d) security ink for anti-counterfeiting application using SrF_2:5% Tb^{3+}, 5% Ce^{3+} nanophosphors before and after 254 nm UV irradiation.

energy transfer from Ce^{3+} ($^5D_{5/2}$) to Tb^{3+} ($^5D_2$) ions. With Ce^{3+} co-doping, Tb^{3+} lifetime increases to 6 ms while Ce^{3+} lifetime decreases from 15.35 and 7.82 ns. The energy transfer efficiency and the spectral overlap integral calculated were found to be 49% and 1.05×10^{10} M^{-1} cm^{-1} nm^4. The synthesized phosphors have excellent biocompatibility towards the HeLa cell line and their cellular uptake was studied. Using the 254 nm wavelength excitation, the applicability of synthesized NPs towards security inks as anti-counterfeiting patterns and forensic fingerprint detection were designed and successfully performed. Thus, the synthesized nanophosphor will have potential applications in different areas, such as security ink, forensic fingerprint detection and *in vitro* bioimaging.

Data availability

All the data are available from the corresponding authors upon request.

Conflicts of interest

There are no conflicts to declare.

Acknowledgements

Authors are grateful to Ranjoy Wangkhem, Nagaland University, Nagaland, for assisting the Photoluminescence facility; Rameshwari Heisnam, Institute of Bioresources and Sustainable Development, Imphal, Manipur; Sophisticated Analytical Instrumentation Centre, Tezpur University for providing facilities for data acquisition.

References

1 R. Grasser, A. Scharmann and K. R. Strack, On the intrinsic nature of the blue luminescence in $CaWO_4$, *J. Lumin.*, 1982, **27**, 263–272.
2 M. Nikl, P. Bohacek, E. Mihokova, A. Vedda, M. Martini, G. P. Pazzi, P. Fabeni, M. Kobayashi and Y. Usuki, Enhanced efficiency of doubly doped $PbWO_4$ scintillator, *Radiat. Eff. Defects Solids*, 2002, **157**, 937–941.
3 H. Q. Wang, M. Batentschuk, A. Osvet, L. Pinna and C. J. Brabec, Rare-Earth Ion Doped Up-Conversion Materials for Photovoltaic Applications, *Adv. Mater.*, 2011, **23**, 2675–2680.
4 S. Sarkar, M. Chatti, V. N. K. B. Adusumalli and V. Mahalingam, Highly Selective and Sensitive Detection of Cu^{2+} Ions Using Ce(III)/Tb(III)-Doped SrF2 Nanocrystals as Fluorescent Probe, *ACS Appl. Mater. Interfaces*, 2015, **7**, 25702–25708.
5 M. Azami, S. Jalilifiroozinezhad, M. Mozafari and M. Rabiee, Synthesis and solubility of calcium fluoride/hydroxy-fluorapatite nanocrystals for dental applications, *Ceram. Int.*, 2011, **37**, 2007–2014.
6 R. Joshi, R. S. Perala, S. B. Shelar, A. Ballal, B. P. Singh and R. S. Ningthoujam, Super Bright Red Upconversion in $NaErF_4$:0.5%Tm@NaYF4:20%Yb Nanoparticles for Anti-

counterfeit and Bioimaging Applications, *ACS Appl. Mater. Interfaces*, 2021, **13**, 3481–3490.
7 W. Cross, T. Blumenthal, J. Kellar, P. S. May, J. Meruga and Q. Luu, Rare-Earth Doped Nanoparticles in Security Printing Applications, *MRS Proc.*, 2012, **1471**, 1270.
8 A. K. Parchur, A. I. Prasad, A. A. Ansari, S. B. Raia and R. S. Ningthoujam, Luminescence properties of Tb^{3+}-doped $CaMoO_4$ nanoparticles: annealing effect, polar medium dispersible, polymer film and core-shell formation, *Dalton Trans.*, 2012, **41**, 11032.
9 G. Phaomei, R. S. Ningthoujam, W. R. Singh, R. S. Loitongbam, N. S. Singh, A. Rath, R. R. Juluri and R. K. Vatsa, Luminescence switching behavior through redox reaction in Ce^{3+} co-doped $LaPO_4$:Tb^{3+} nanorods: Re-dispersible and polymer film, *Dalton Trans.*, 2011, **40**, 11571–11580.
10 N. S. Singh, N. K. Sahu and D. Bahadur, Multicolor tuning and white light emission from lanthanide doped $YPVO_4$ nanorods: energy transfer studies, *J. Mater. Chem. C*, 2014, **2**, 548–555.
11 N. Yaiphaba, Effect of Ce^{3+} Co-doping on $GdPO_4$:Tb^{3+} Nanoparticles: Photoluminescence and Energy Transfer Studies, *Asian J. Chem.*, 2021, **33**, 903–908.
12 Q. Luo, X. Qiao, X. Fan and X. Zhang, Preparation and luminescence properties of Ce^{3+} and Tb^{3+} co-doped glasses and glass ceramics containing SrF_2 nanocrystals, *J. Non-Cryst. Solids*, 2010, **356**, 2875–2879.
13 Q. Luo, X. Qiao, X. Fan and X. Zhang, Photoluminescence and efficient energy transfer from Ce^{3+} to Tb^{3+} or Mn^{2+} in $Ca_9ZnLi(PO_4)_7$ host, *Appl. Phys. A: Mater. Sci. Process.*, 2012, **108**, 569–576.
14 L. Wang, Y. Xu, D. Wang, R. Zhou, N. Ding, M. Shi, Y. Chen, Y. Jiang and Y. Wang, Deep red phosphors $SrAl_{12}O_{19}$:Mn^{4+}, M (M = Li^+, Na^+, K^+, Mg^{2+}) for high colour rendering white LEDs, *Phys. Status Solidi A*, 2013, **210**, 1433–1437.
15 W. Tang, S. Ding, Y. Yuan and G. Xie, Effect of $Ce3^+$ and $Tb3^+$ codoping on luminescence properties of $Na_3SrMg_{11}(PO_4)_9$:Eu^{2+} phosphors, *Opt. Mater.*, 2020, **106**, 110003.
16 D. Jia, X. J. Wang, W. Jia and W. M. Yen, Persistent energy transfer in $CaAl_2O_4$:Tb^{3+}, Ce^{3+}, *J. Appl. Phys.*, 2003, **93**, 148–152.
17 W. He, H. Du, J. Fu, F. Luan, D. Li, L. Sun and D. Guo, Efficient energy transfer from Ce^{3+} to Tb^{3+} in BaF_2: green-emitting phosphors for potential applications in the detection of Cu^{2+} ions, *New J. Chem.*, 2021, **45**, 1446–1455.
18 N. Kumam, N. P. Singh, L. P. Singh and S. K. Srivastava, Enhancement of luminescence in white emitting strontium fluoride core @ calcium fluoride shell nanoparticles, *Nanoscale Res. Lett.*, 2015, **10**, 6–13.
19 B. Xu, H. He, Z. Gu, S. Jin, Y. Ma and T. Zhai, Improving 800 nm Triggered Upconversion Emission for Lanthanide-Doped CaF_2 Nanoparticles through Sodium Ion Doping, *J. Phys. Chem. C*, 2017, **121**, 18280–18287.
20 N. P. Singh, N. Kumam, L. P. Singh, N. R. Singh and S. K. Srivastava, Luminescent enhancement study of 3Tb,5Ce,5Li: CaF_2: effect of Li^+ ion concentration and hyperthermia applications of 3Tb:CaF2/Fe3O4 nanocomposite, *New J. Chem.*, 2019, **43**, 1328–1339.
21 R. B. Hughes-Currie, K. V. Ivanovskikh, J. P. R. Wells, M. F. Reid, R. A. Gordon, L. Seijo and Z. Barandiarán, X-ray Excitation Triggers Ytterbium Anomalous Emission in CaF_2:Yb but Not in SrF_2:Yb, *J. Phys. Chem. Lett.*, 2017, **8**, 1175–1178.
22 R. N. Grass and W. J. Stark, Flame synthesis of calcium-, strontium-, barium fluoride nanoparticles and sodium chloride, *Chem. Commun.*, 2005, 1767–1769.
23 C. Zhang, Z. Hou, R. Chai, Z. Cheng, Z. Xu, C. Li, L. Huang and J. Lin, Mesoporous SrF_2 and SrF_2:Ln^{3+} (Ln = Ce, Tb, Yb, Er) Hierarchical Microspheres: Hydrothermal Synthesis, Growing Mechanism, and Luminescent Properties, *J. Phys. Chem. C*, 2010, **114**, 6928–6936.
24 A. A. Ansari, A. K. Parchur, B. Kumar and S. B. Rai, Highly aqueous soluble CaF2:Ce/Tb nanocrystals: effect of surface functionalization on structural, optical band gap, and photoluminescence properties, *J. Mater. Sci.: Mater. Med.*, 2016, **27**, 1–11.
25 D. Przybylska, A. Ekner-Grzyb, B. F. Grześkowiak and T. Grzyb, Upconverting SrF_2 nanoparticles doped with Yb^{3+}/Ho^{3+}, Yb^{3+}/Er^{3+} and Yb^{3+}/Tm^{3+} ions – optimisation of synthesis method, structural, spectroscopic and cytotoxicity studies, *Sci. Rep.*, 2019, **9**, 1–12.
26 M. Quintanilla, I. X. Cantarelli, M. Pedroni, A. Speghini and F. Vetrone, Intense ultraviolet upconversion in water dispersible SrF_2:Tm^{3+},Yb^{3+} nanoparticles: the effect of the environment on light emissions, *J. Mater. Chem. C*, 2015, **3**, 3108–3113.
27 S. Balabhadra, Upconverting Nanoparticles Working As Primary Thermometers In Different Media, *J. Phys. Chem. C*, 2017, **121**, 13962–13968.
28 Y. Yan, Y. Tan, D. Li, F. Luan and D. Guo, Efficient energy transfer, multi-colour emitting and temperature sensing behavior of single-phase Tb^{3+}, Eu^{3+} co-doped strontium fluoride phosphors, *J. Lumin.*, 2019, **211**, 209–217.
29 K. Shwetabh, M. M. Upadhyay and K. Kumar, Synthesis and upconversion emission studies of CaYF5:Ho^{3+}/Yb^{3+} phosphor and its applications in optical thermometry, fingerprint detection, and security ink, *RSC Adv.*, 2023, **13**, 9377–9386.
30 J. Liang, T. Fan, J. T. Lü, T. Guan, T. T. Deng and B. Xiong, Dual-mode luminescence anti-counterfeiting and white light emission of $NaGdF_4$:Ce,Eu,Tb/carbon dot hydrophilic nanocomposite ink, *RSC Adv.*, 2023, **13**, 25681–25690.
31 Y. Jin, Hydrothermal Synthesis and Luminescent Properties of (Sr, Ba)F_2:Eu^{3+} Nanostructures, *J. Nanosci. Nanotechnol.*, 2016, **16**, 9856–9861.
32 M. Karimi, S. Hesaraki and N. Nezafati, *In vitro* biodegradability–bioactivity-biocompatibility and antibacterial properties of SrF2 nanoparticles synthesized by one-pot and eco-friendly method based on ternary strontium chloride-choline chloride-water deep eutectic system, *Ceram. Int.*, 2018, **44**, 12877–12885.
33 R. K. Sharma, S. Nigam, Y. N. Chouryal, S. Nema, S. P. Bera, Y. Bhargava and P. Ghosh, Eu-Doped BaF_2 Nanoparticles for Bioimaging Applications, *ACS Appl. Nano Mater.*, 2019, **2**, 927–936.
34 M. B. Hansen, S. E. Nielsen and K. Berg, Re-examination and further development of a precise and rapid dye, *J. Immunol. Methods*, 1989, **119**, 203–210.

35 T. Mosmann, Rapid Colorimetric Assay for Cellular Growth and Survival: Application to Proliferation and Cytotoxicity Assays, *J. Immunol. Methods*, 1983, **65**, 55–63.
36 B. Chazotte, Labeling Nuclear DNA Using DAPI, *Cold Spring Harb. Protoc.*, 2011, 80–82.
37 R. D. Shannon, Revised Effective Ionic Radii and Systematic Studies of Interatomic Distances in Halides and Chalcogenides, *Acta Crystallogr. Sect. A*, 1976, **32**, 751–767.
38 L. Van Pieterson, M. F. Reid, R. T. Wegh, S. Soverna and A. Meijerink, $4fn \rightarrow 4f^{n-1}$ $5d$ transitions of the light lanthanides: Experiment and theory, *Phys. Rev. B: Condens. Matter Mater. Phys.*, 2002, **65**, 1–16.
39 L. R. K. T. Jacob, Shubhra Raj, Vegard's law: a fundamental relation or an approximation?, *Int. J. Mater. Res.*, 2007, **98**, 776–779.
40 B. V. Ratnam, M. Jayasimhadri, J. Yoon, K. Jang, H. S. Lee, S. S. Yl, S. H. Kim and J. H. Jeong, Luminescent Properties of Tb^{3+}-Doped $NaCaPO_4$ Phosphor, *J. Korean Phys. Soc.*, 2009, **55**, 2383–2387.
41 W. Kemp, *Organic Spectroscopy*, Macmillan Educational Ltd, Houldmills, Hampshire, 1987.
42 A. K. Thottoli and A. K. A. Unni, Effect of trisodium citrate concentration on the particle growth of ZnS nanoparticles, *J. Nanostructure Chem.*, 2013, **3**, 1.
43 T. Demkiv, M. Chylii, V. Vistovskyy, A. Zhyshkovych, N. Gloskovska, P. Rodnyi, A. Vasil'ev, A. Gektin and A. Voloshinovskii, Intrinsic luminescence of SrF_2 nanoparticles, *J. Lumin.*, 2017, **190**, 10–15.
44 N. Bhunia, M. Bhar and P. Mukherjee, Maximizing Terbium-Europium Electronic Interaction: Insight from Variation of Excitation Energy, *J. Phys. Chem. C*, 2023, **127**, 6425–6438.
45 M. S. Bhadane, K. H. Gavhane, V. S. Ghemud, S. S. Dahiwale, P. S. Patil and S. D. Dhole, A post annealing effect on SrF_2 nanoparticles: Structural, morphological, functional and dosimetric properties, *J. Alloys Compd.*, 2020, **846**, 156343.
46 D. D. Yengkhom, G. S. Ningombam, R. Heisnam, N. Sharma, R. S. Nongmaithem and F. A. S. Chipem, Luminescence enhancement and tunable color emission in Eu/Dy/Sm codoped $CaW_{1-x}Mo_xO_4$ phosphor, *Inorg. Chem. Commun.*, 2022, **141**, 1–10.
47 N. K. Sahu, N. S. Singh, L. Pradhan and D. Bahadur, Ce^{3+} sensitized $GdPO_4$:Tb^{3+} with iron oxide nanoparticles: a potential biphasic system for cancer theranostics, *Dalton Trans.*, 2014, **43**, 11728–11738.
48 T. C. Dexter, A Theory of Sensitized Luminescence in Solids, *J. Chem. Phys.*, 1953, **21**, 836–850.
49 S. Wang, B. Devakumar, Q. Sun, J. Liang, L. Sun and X. Huang, Highly efficient near-UV-excitable $Ca_2YHf_2Al_3O1_2$:Ce^{3+},Tb^{3+} green emitting garnet phosphors with potential application in high-color rendering warm-white LEDs, *J. Mater. Chem. C*, 2020, **8**, 4408–4420.
50 L. Sun, B. Devakumar, J. Liang, S. Wang, Q. Sun and X. Huang, Highly efficient $Ce^{3+} \rightarrow Tb^{3+}$ energy transfer induced bright narrowband green emissions from garnet-type $Ca_2YZr_2(AlO_4)_3$:Ce^{3+},Tb^{3+} phosphors for white LEDs withhigh color rendering index, *J. Mater. Chem. C*, 2019, **7**, 10471–10480.
51 J. R. Lakowicz, *Principles of Fluorescence Spectroscopy*, Springer, Singapore, 3rd edn, 2006.
52 G. Blasse, Energy transfer in oxidic phosphors, *Phys. Lett. A*, 1968, **28**(6), 444–445.
53 (*a*) O. S. Singh, R. Wangkhem, N. Yaiphaba, T. D. Singh and N. S. Singh, Bi^{3+} sensitized Gd_2O_3:Eu^{3+}: A potential red phosphor for UV LED pumped white light emission, *J. Alloys Compd.*, 2022, **902**, 163831; (*b*) T. S. Singh and S. Mitra, Interaction of cinnamic acid derivatives with serum albumins: A fluorescence spectroscopic study, *Spectrochim. Acta A*, 2011, **78**, 942–948.
54 D. Durmus, Correlated color temperature: Use and limitations, *Light. Res. Technol.*, 2022, **54**, 363–375.